Kinetics and Nucleation for Driven Thin Film Flow

Rachel Levy and Michael Shearer*

April 1, 2004

1 Introduction

The theory of scalar conservation laws that includes a kinetic relation and nucleation condition, formulated in [9], is motivated by models of the flow of thin liquid films. It applies to equations

$$h_t + f(h)_x = 0, \tag{1.1}$$

in which the flux $f : \mathbb{R} \to \mathbb{R}$ is non-convex. Here $h = h(x, t)$ represents the height of the free surface of the film flowing over a solid substrate. The kinetic relation describes admissible nonclassical shock waves, known as undercompressive shocks, and the nucleation condition determines when a nonclassical solution is selected.[1] The hyperbolic theory is able to capture features observed in thin film flow, such as multiple long-time solutions for the same initial upstream and downstream states. This is an unexpected feature of the hyperbolic theory, where generally long-time behavior is uniquely determined by the two limits $\lim_{x\to\pm\infty} h(x, 0)$, the detailed intermediate structure being washed out by wave interactions.

The novelty in this hyperbolic theory is the use of a nucleation condition, which previously had been used only in the context of phase transitions (modeled by systems of mixed hyperbolic-elliptic type [1]), where non-uniqueness of solutions of initial value problems is unavoidable without it[2]. By contrast, for scalar conservation laws, and indeed for hyperbolic systems of conservation laws, there is an extensive theory with kinetics [10], in which the nonclassical solution is taken in preference to the classical whenever it is available, thereby dispensing with the need for a separate nucleation condition, while retaining the property of uniqueness. Such a selection rule is consistent with the consideration of traveling waves for equation (1.1) regularized by second order diffusion and third order dispersion, as in the modified KdV-Burgers equation ([5, 6, 10]), and for the hyperbolic p-system regularized with viscosity and capillarity ([14, 16]). However, this simple selection rule is inadequate for some applications involving thin liquid films in which surface tension provides a fourth order dissipation; in this paper we show that the nucleation condition provides the appropriate selection criterion.

*Department of Mathematics and Center for Research in Scientific Computation, North Carolina State University Raleigh, NC 27695. Research supported by NSF Grants DMS-9803305, DMS-0244491.

[1] The term *classical* refers here to solutions described by the theory of Lax, Oleinik, Kruzkov [7, 8, 12]. Classical shocks are required to satisfy the Lax entropy conditions.

[2] Except for an extreme choice of kinetic relation [17].

The context we discuss is the flow of a thin liquid film up an inclined planar solid substrate, the flow being driven by a surface tension gradient against the action of gravity. (Another thin film scenario with similar behavior is discussed in [15].) For our application, the equation with surface tension can be written (after nondimensionalization) as

$$h_t + f(h)_x = -\gamma(h^3 h_{xxx})_x, \quad h = h(x,t) \in (0,1),\ x \in \mathbb{R},\ t > 0, \tag{1.2}$$

with $f(h) = h^2 - h^3$. A surface tension parameter $\gamma > 0$ is included for the purpose of discussing the singular limit $\gamma \to 0$. In this paper, we explore the connection between the hyperbolic theory and equation (1.2) in detail. The kinetic relation, describing both undercompressive and so-called reverse undercompressive shocks, and the nucleation condition, are formulated in terms of traveling wave solutions of (1.2). For the kinetic relation, this is standard procedure, although analysis of the third order ODE describing traveling waves is limited, so that we are forced to rely partly on numerical results. The nucleation condition has not been formulated before in terms of traveling waves. However, for equation (1.2), there is a natural nucleation condition dictated by properties of traveling waves. It states that nucleation takes place for initial data, specifically, upstream and downstream heights, for which there is no traveling wave (and no rarefaction wave) connecting those heights. For such data, the PDE has to select a long-time solution which is not a traveling wave, and it appears to do so by *nucleating* a broadening capillary ridge (where h is roughly constant), separating an undercompressive wave and a classical wave.[3]

Having formulated the kinetic relation and nucleation condition, numerical and analytical results are combined to solve the Riemann problem for (1.1), leading to approximation of solutions of the Cauchy problem by wave front tracking.

It would be too much to expect the hyperbolic theory to predict long time behavior of equation (1.2) for $\gamma > 0$ for all initial data. To probe the limit $\gamma \to 0$ (where the hyperbolic theory should apply), we consider specific initial data to determine the effect of surface tension on the interaction of waves. Using numerical experiments, we observe that the surface tension sets a length scale below which surface tension can interfere with the predicted nonlinear hyperbolic wave interaction. This helps explain earlier observations concerning the dependence of the time-asymptotic structure on the initial data: it was found in [2] that for certain initial data with a single ridge, it is possible to generate a long-time double wave structure, by simply broadening the width of the initial ridge. Of course, such broadening would not affect the hyperbolic equation, aside from lengthening the time before the first wave interaction, but for equation (1.2) the width is significant. Equivalently, keeping the width constant, we can decrease γ, recovering the hyperbolic behavior for small enough γ.

2 Hyperbolic Theory

Consider the scalar conservation law

$$\partial_t h + \partial_x f(h) = 0, \quad h = h(x,t) \in (0,1),\ x \in \mathbb{R},\ t > 0, \tag{2.1}$$

[3]Here, the waves appear as approximate smooth traveling waves that steepen and become shocks as $\gamma \to 0$.

where $f(h) = h^2 - h^3$. Note that $f(h) > 0$, f has an inflection point at $h = 1/3$, and f has a maximum at $h = 2/3$. Smooth solutions $h(x,t)$ are constant on *characteristics*, which are straight lines in the $x - t$ plane of space-time, with characteristic speed $f'(h)$.

A **shock wave from h_- to h_+** is a weak solution $h = h(x,t)$ that is piecewise smooth near a discontinuity $x = \hat{x}(t)$, with one-sided limits $h_\pm = h(\hat{x}(t)\pm, t)$. We shall generally deal with piecewise constant shock waves, for which h_- and h_+ are constant and the shock speed $s = \hat{s}(h_-, h_+) = \hat{x}'$ (also constant) is given by the Rankine-Hugoniot condition $s(h_+ - h_-) = f(h_+) - f(h_-)$; thus

$$\hat{s}(h_-, h_+) = \frac{f(h_-) - f(h_+)}{h_- - h_+} = h_- + h_+ - h_-^2 - h_- h_+ - h_+^2.$$

A shock wave from h_- to h_+ is a **classical shock**[4] if it satisfies the *Lax shock inequalities* [8]:

$$f'(h_+) \le \hat{s}(h_-, h_+) \le f'(h_-).$$

These inequalities mean that characteristics $x = f'(h_\pm)t + \text{const.}$ approach the shock wave on both sides. By contrast, in a **nonclassical shock**, the characteristics pass through the shock from downstream (ahead of the shock) to upstream:

$$\hat{s}(h_-, h_+) \ge f'(h_-) \text{ and } \hat{s}(h_-, h_+) \ge f'(h_+).$$

As in [9, 10], we consider equation (2.1) supplemented by a single **entropy inequality**

$$\eta(h)_t + q(h)_x \le 0 \tag{2.2}$$

in the weak sense, where η, q is a specific entropy-entropy flux pair: $\eta : (0,1) \to \mathbb{R}$ is convex and $q : (0,1) \to \mathbb{R}$ is related to η by compatibility with the conservation law (2.1):

$$q'(h) = f'(h)\,\eta'(h).$$

The entropy inequality (2.2) gives an additional restriction on shock waves as follows. We define the *entropy dissipation function* $E : (0,1) \times (0,1) \to \mathbb{R}$ by

$$E(h_-, h_+) = -\hat{s}(h_-, h_+)\,(\eta(h_+) - \eta(h_-)) + q(h_+) - q(h_-).$$

Then the entropy inequality (2.2) holds on a shock wave from h_- to h_+ if and only if

$$E(h_-, h_+) \le 0. \tag{2.3}$$

In particular, all classical shocks automatically satisfy (2.3), so the inequality is a restriction only on nonclassical shocks. Equality in (2.3) is associated with the **zero entropy dissipation function** $h^* : (0,1) \to (0,1)$, satisfying

$$E(h^*(h_+), h_+) = 0, \quad h^*(h_+) \ne h_+ \text{ for } h_+ \ne 1/3, \quad \text{and} \quad h^* \circ h^*(h_+) = h_+. \tag{2.4}$$

In order for initial value problems to be well-posed, we have to specify which nonclassical shocks will be admissible.[5] As in [9, 10], we specify admissible shocks using a kinetic relation. In the

[4] The terms *compressive shock* and *classical shock* are used interchangeably.

[5] The entropy inequality does not serve this purpose - it represents only a constraint on the specification of admissible nonclassical shocks. In Section 3, where admissibility is motivated by a traveling wave condition, we exhibit a natural choice of entropy-entropy flux pair.

thin film context, this involves specifying a monotonically decreasing Lipschitz continuous *kinetic function* $h^K : (0,1) \to (0,1)$ with the property that

$$\begin{aligned} \tfrac{1}{2}(1-h) \;\le\; h^K(h) \;&<\; h^*(h) \qquad\qquad h < \tfrac{1}{3}, \\ h^*(h) \;<\; h^K(h) \;&\le\; \tfrac{1}{2}(1-h), \qquad h > \tfrac{1}{3}. \end{aligned} \tag{2.5}$$

Note that the line from $(h, f(h))$ to $\left(\frac{1}{2}(1-h), f(\frac{1}{2}(1-h))\right)$ is tangent to the graph of f at the latter point. The function h^K specifies undercompressive (i.e., admissible nonclassical) shocks as follows:

A shock from h_- to h_+ is *undercompressive* if $h_- = h^K(h_+)$.

This description of admissible nonclassical shocks is known as the **Kinetic Relation** [9]. In the next section, we determine a suitable function h^K by examining traveling wave solutions of the full PDE (1.2), but in fact the hyperbolic theory can be developed for rather general choice of function h^K. Undercompressive shocks have the important property that the downstream height h_+ uniquely determines the upstream height h_- and therefore the shock speed.

A **rarefaction wave** is a continuous solution $h(x,t) = U(x/t)$ of equation (2.1) given by the implicit formula

$$f'(U(\xi)) = \xi. \tag{2.6}$$

Consequently, since $\xi = x/t$ is increasing, a rarefaction wave can join two constant states h_-, h_+ if and only if $h_- < h_+ < 1/3$, or $1/3 < h_+ < h_-$:

$$h(x,t) = \begin{cases} h_-, & x < f'(h_-)t \\ U(x/t), & f'(h_-)t < x < f'(h_+)t \\ h_+, & x > f'(h_+)t. \end{cases} \tag{2.7}$$

The **Riemann problem** is the initial value problem for equation (2.1), in which the initial data consist of two constants:

$$h(x,0) = \begin{cases} h_L, & x < 0, \\ \\ h_R, & x > 0. \end{cases} \tag{2.8}$$

The solution of the Riemann problem will be a weak solution of (2.1,2.8) constructed from constants, rarefaction waves, and admissible shocks. The difficulty is that if we allow all classical shocks, undercompressive shocks and rarefaction waves in the solution of the Riemann problem, then for many choices of initial data, there are two solutions, one involving only a classical shock or rarefaction wave, the other having both a classical (shock or rarefaction) wave and an undercompressive shock. Both of these solutions have a role in the long-time behavior of solutions of initial value problems, but in order to have a well-posed initial value problem for equation (2.1), we have to select a unique solution from the two possible solutions, for each choice of h_L, h_R.

It is natural to base the selection of a unique solution on a Lipschitz continuous *nucleation function* $h^N : (0,1) \to (0,1)$. The natural restrictions on h^N relate to the *middle equilibrium function,* defined as $h^m(h) = 1 - h - h^K(h)$:

$$\begin{aligned} h^m(h) \le h^N(h) < \tfrac{1}{2}(1-h), \quad h < 1/3 \\ h^m(h) \ge h^N(h) > \tfrac{1}{2}(1-h), \quad h > 1/3. \end{aligned} \tag{2.9}$$

Then the **Nucleation Condition** is: *The solution of the Riemann problem is classical if and only if:*

$$h_R < 1/3 \text{ and } h_L < h^N(h_R), \quad \text{or} \quad h_R > 1/3 \text{ and } h_L > h^N(h_R). \tag{2.10}$$

In the special case: $h^N = h^m$ (cf. [6, 10]), classical shocks lose admissibility at precisely the shock speed of an undercompressive shock. The nonclassical solution of the Riemann problem is then selected whenever it is available. For the thin film PDE (1.2), this redundant choice of nucleation condition does not allow solutions of the hyperbolic conservation law to capture all of the wave structures observed in the full PDE [2].

Now we are ready to specify the solution of the Riemann problem with kinetics and nucleation. The construction is the same as in [9], except for the restriction to the interval $(0, 1)$. In Fig. 2.1 we show schematically the waves in the solution for each choice of data (h_L, h_R). In the Figure, the different wave combinations are separated by the *kinetic curve* $h_L = h^K(h_R)$, by the *nucleation curve* $h_L = h^N(h_R)$, which, together with the line $h_R = 1/3$, separates classical from nonclassical solutions, and by the line $h_L = h_R$.

Not all of the details shown in the figure are needed to specify a unique solution of the Riemann problem for all data. For example, we show the nucleation and kinetic curves both emanating from the point $(0, 1)$. In fact, they may be attached to the line $h_R = 1$ at points $h_L > 0$. However, when the kinetic and nucleation functions are determined from considering traveling waves of the system with surface tension, then these curves are attached as shown in the Figure. Interestingly, this is not true at the other end of these curves (where $h_R = 0$); they are not constrained to be attached to the corners of the domain, and numerical results do not resolve whether or not they are, so they are shown in the Figure as being attached at points $(h_L, 0)$, with $0 < h_L < 1$.

In Fig. 2.2 we show the solution in another way, to demonstrate how it is constructed. In this Figure, we also show the construction of the double shock structure, by indicating a specific h_L in the interval labeled CU, corresponding to a solution with a classical shock and an undercompressive shock. The speeds of the two waves are the slopes of the dashed chords shown between h_L and $h^K(h_R)$ (for the classical shock), and between $h^K(h_R)$ and h_R (for the undercompressive shock).

It is worth noting that the solution $h(x, t)$ of the Riemann problem lies in the interval $(0, 1)$ for any data in $(0, 1) \times (0, 1)$. Consequently, the existence theorem of [9] can be adapted to the present context to prove that for arbitrary initial data $h(x, 0) = h_0(x)$ in BV, there is a solution of the Cauchy problem constructed using wave front tracking and the Riemann problem solutions of Fig. 2.1. Moreover, the solution $h(x, t)$ remains in the interval $(0, 1)$ for all x and $t > 0$.

3 Traveling Waves

In this section, we use traveling wave solutions of (1.2) to define specific kinetic and nucleation functions. We seek traveling wave solutions, $h(x, t) = \tilde{h}((x - st)/\gamma^{\frac{1}{3}})$ of (1.2), in which s is the speed of the traveling wave. Note that if a trajectory $\tilde{h}(\xi)$ satisfies boundary conditions $\tilde{h}(\pm\infty) = h_\pm$, then as $\gamma \to 0+$, the PDE solutions $h(x, t)$ approach the shock from h_- to h_+ with speed s.

By substitution into the PDE (1.2) and one integration, we arrive at a third order ordinary differ-

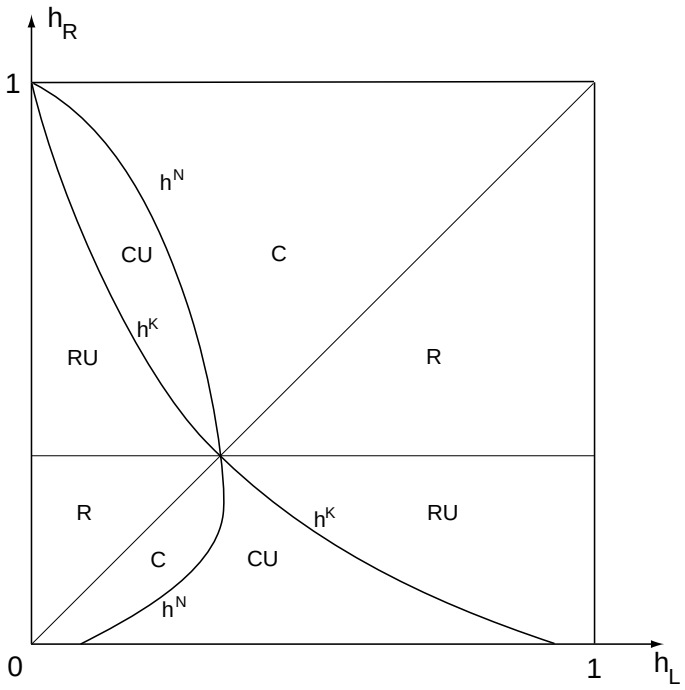

Figure 2.1: Solution of the Riemann Problem. C: classical shock, U: undercompressive shock; R: rarefaction wave.

ential equation for $h(\xi)$ (dropping the tilde), where $\xi = (x - st)/\gamma^{\frac{1}{3}}$:

$$h''' = \frac{sh - f(h) - sh_0 + f(h_0)}{h^3}, \tag{3.11}$$

in which $h_0 > 0$ is the downstream or upstream height. Equation (3.11) is equivalent to the first order system

$$\begin{aligned} h' &= u \\ u' &= v \\ v' &= g(h), \end{aligned} \tag{3.12}$$

where

$$g(h) = \frac{sh - f(h) - sh_0 + f(h_0)}{h^3}.$$

Equilibria of the system are of the form $(h, u, v) = (\bar{h}, 0, 0)$ with $g(\bar{h}) = 0$, i.e.,

$$s(\bar{h} - h_0) = f(\bar{h}) - f(h_0). \tag{3.13}$$

For fixed h_0 and s, equilibria $(h, 0, 0)$ for equation (3.13) are represented by intersections of a straight line with slope s through $(h_-, f(h_-))$ and the graph of the cubic flux function $f(h)$. Each pair of intersections h_1, h_2 represents a shock wave from h_1 to h_2 (or h_2 to h_1) with speed s. Accordingly, we are interested only in the situation in which there are three (or in limiting cases, two) intersections. When there are three equilibria, we label them B (bottom), M (middle) and T (top), and label the three corresponding values of h as h_b, h_m, h_t. Observe that

$$h_b + h_m + h_t = 1, \tag{3.14}$$

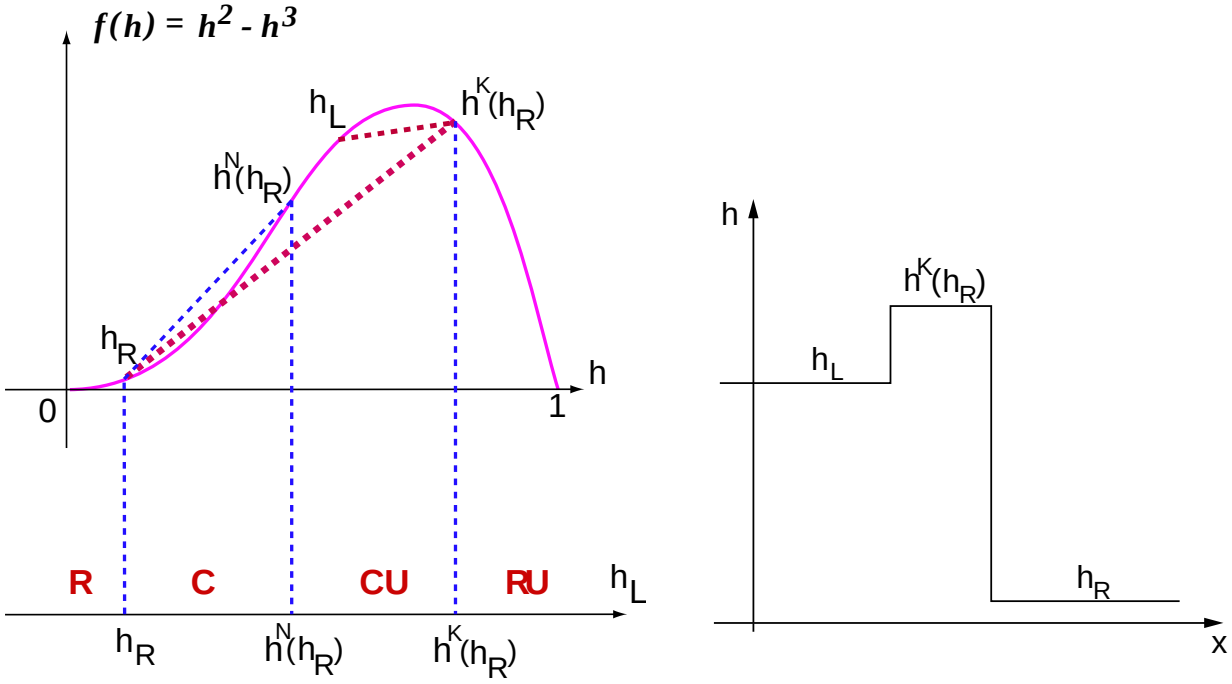

Figure 2.2: Solution of the Riemann Problem for fixed $h_R < 1/3$

which indeed motivates the definition of the middle equilibrium function h^m of the last section.

The linearized equations show that B and T have one-dimensional unstable manifolds $W^U(B)$, $W^U(T)$ and two-dimensional stable manifolds $W^S(B)$, $W^S(T)$. Similarly, M has a two-dimensional unstable manifold $W^U(M)$ and one-dimensional unstable manifold $W^U(M)$.

In our discussion of traveling waves, we are particularly interested in the possibility of *undercompressive waves*, which correspond to trajectories from T to B, and *reverse undercompressive waves*, which correspond to trajectories from B to T. Both types of trajectories, or heteroclinic orbits, occur only for special values of parameters; they are co-dimension one. We express this fact in the following theorem, appealing to [2] for much of the proof.

Theorem 3.1 *For each $h_b < 1/3$, there are values h_1, h_2 of h with $1/3 < h_1 < h_2$ such that there is an undercompressive wave from h_1 to h_b, and a reverse undercompressive wave from h_b to h_2.*

Proof. The proof of existence of h_1 (for undercompressive waves) is given in [2]. For reverse undercompressive waves, the argument to give the existence of h_2 is very similar; we omit the details.

To show that $h_1 < h_2$, we use the Lyapunov function

$$L(h) = h'h'' + G(h), \tag{3.15}$$

where $G(h) = -\int^h g(y)\,dy$. Then

$$L(h)' = (h'')^2 \geq 0. \tag{3.16}$$

In particular, for undercompressive waves from h_1 to h_b, we must have $G(h_1) < G(h_b)$, whereas for reverse undercompressive waves, from h_b to h_2, we have the reverse inequality $G(h_2) > G(h_b)$. Thus for a fixed h_b, as in the theorem, the corresponding values of h_1, h_2 for undercompressive and reverse undercompressive waves lie on opposite sides of the value $h^* = h^*(h_b)$, defined by $G(h^*) = G(h_b),\ h_b \neq h^*$.

From the definitions of g and G, we obtain the formula

$$G(h) = \log h - h + \frac{s}{h} - \frac{K}{2h^2}, \tag{3.17}$$

where $K = sh_0 + h_0^3 - h_0^2$. Now consider $h_0 = h_b$, and let h_t correspond to the top equilibrium (i.e., h_1 or h_2 in the theorem). Then we easily calculate, using $s = \hat{s}(h_b, h_t)$,

$$K = h_t h_b h_m, \tag{3.18}$$

where $h_m = 1 - h_b - h_t$ is the middle equilibrium.

Now define $\phi(h_t) = G(h_t) - G(h_b)$, where we consider h_b to be fixed. Then, taking into account that both s and K depend on h_t, we calculate

$$\phi'(h_t) = \frac{1}{2h_b h_t^2}(2h_t + h_b - 1)(h_t - h_b)^2$$

Thus, $\phi'(h_t) > 0$ for $h_t > \frac{1}{2}(1 - h_b)$. But this is precisely the range for h_t; the value $h_t = \frac{1}{2}(1 - h_b)$ is where the line from $(h_b, f(h_b))$ to $(h_t, f(h_t))$ is tangent at h_t. Consequently, $G(h_t) > G(h_b)$ for $h_t > h^*(h_b)$, so $h_2 > h^*(h_b) > h_1$. ■

We can identify the inequality

$$G(h_+) > G(h_-), \tag{3.19}$$

necessary for the existence of a traveling wave from h_- to h_+, with an entropy inequality (2.2). Let

$$\eta(h) = \frac{1}{2h}; \qquad q(h) = \frac{3}{2}h - \log h. \tag{3.20}$$

Then, with $f(h) = h^2 - h^3$, it is easy to check that

$$q'(h) = \eta'(h) f'(h),$$

so that indeed, η, q are an entropy-entropy flux pair for the equation (2.1), meaning that across classical shocks from h_- to h_+ with speed s,

$$-s(\eta(h_+) - \eta(h_-)) + q(h_+) - q(h_-) \leq 0, \tag{3.21}$$

since $\eta(h)$ is convex. In fact, inequality (3.21) is precisely the same as the necessary condition (3.19) for a traveling wave, so that it is satisfied by any nonclassical shock possessing a traveling wave.

Equality in (3.21), defines the zero entropy dissipation function $h_- = h^*(h_b)$, with $h^* : (0,1) \to (0,1)$ (see (2.4)). We can find a useful parameterization of h^* as follows. After some manipulation, we find that

$$\begin{aligned} G(h_+) - G(h_-) &= \frac{h_+ - h_-}{2h_+h_-}[(h_+ - h_-)^2 - (h_+ - h_-)] + \log\frac{h_+}{h_-} \\ &= \frac{y-1}{2}\left[h_+\frac{(1-y)^2}{y^2} - \frac{1+y}{y}\right] + \log y, \qquad y = \frac{h_+}{h_-}. \end{aligned} \tag{3.22}$$

The final expression is linear in h_+. Thus, the curve $G(h_+) = G(h_-)$ is given parametrically by

$$h_+ = F(y); \quad h_- = F(y)/y, \qquad F(y) = \frac{y^2}{(1-y)^2}\left[\frac{1+y}{y} + \frac{2}{1-y}\log y\right], \quad 0 < y < \infty. \tag{3.23}$$

Here, $F : (0, \infty) \to \mathbb{R}$ has the following properties:

1. $\lim_{y\to\infty} F(y) = 1$; $\lim_{y\to 0+} F(y) = 0$;

2. $\lim_{y\to 1} F(y) = \frac{1}{3}$.

The curve is symmetric about the diagonal $h_- = h_+$, and a lengthy calculation shows that it is monotonic. Therefore, we can express h_- as a monotonically decreasing function $h_- = h^*(h_+)$ of h_+. Then $h^*(1) = 0$, $h^*(1/3) = 1/3$ and $h^*(0) = 1$. Consequently, for the reverse undercompressive waves, we conclude that $h^K(h_R)$ approaches zero as h_R approaches one. This is clearly shown in the numerical results of Fig. 3.3. However, this does not work the same way for undercompressive waves. We cannot conclude that $h^K(h_R)$ approaches one as $h_R \to 0$. The numerical results of Fig. 3.3 are not definitive on this point.

Regarding the nucleation condition, the function $h^N(h_R)$ records the value of h at the middle equilibrium on the boundary between the existence and non-existence of traveling waves from M to B (when $h_R < 1/3$), and from M to T (when $h_R > 1/3$). (These two cases are referred to as *jump-down* and *jump-up*.) However, because of the way Theorem 3.1 is formulated, we chose to fix $h_b < 1/3$ and to calculate the nucleation threshold for both types of trajectory by varying h_m. Thus, the middle equilibrium h_m is calculated as a function of h_b, which is the same as h_R only for $h_R < 1/3$. To compute $h^N(h_R)$ for $h_R > 1/3$, we have to process the data shown in Fig 3.4, leading to the function shown schematically in Figure 2.1, and numerically in Fig 4.7.

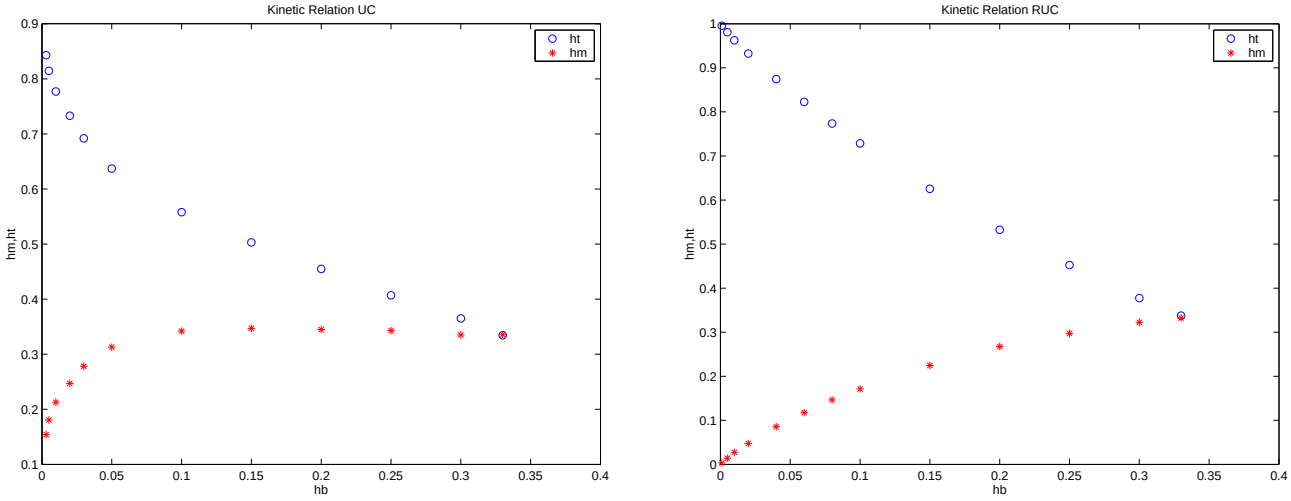

Figure 3.3: Kinetic relation for undercompressive shocks (left) and for reverse undercompressive shocks (right).

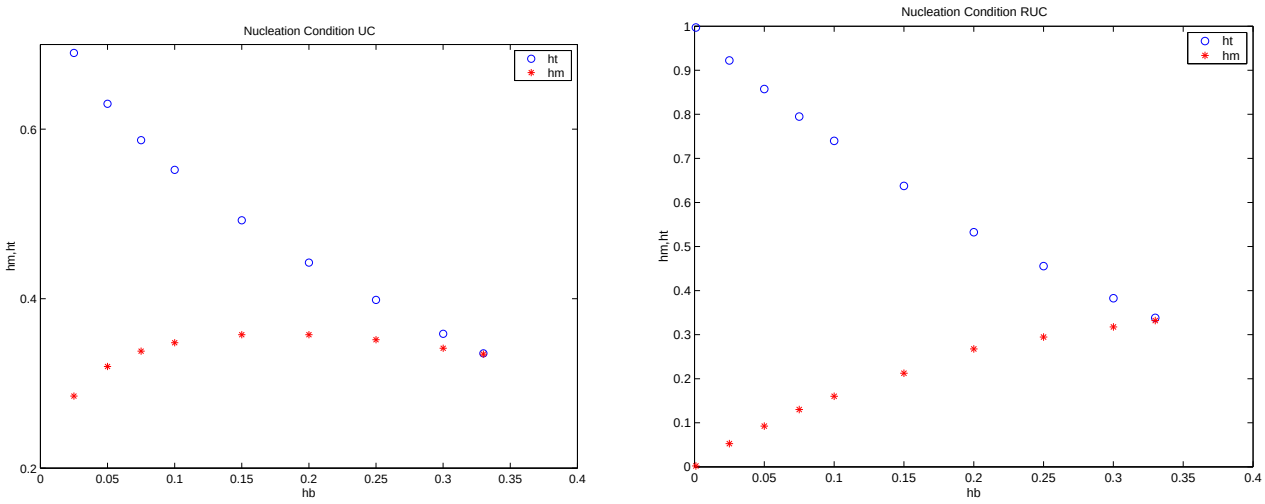

Figure 3.4: Nucleation Condition: Jump-down case (left); jump-up case (right).

4 Numerical Simulations

To compute the kinetic relation and nucleation condition described in the previous section, we calculate trajectories for the system of ODE (3.12). The computational results are used to generate a numerical version of the map of the Riemann solver, Fig. 2.1. These numerical results are given in Subsection 4.1. In Subsection 4.2, we show numerical simulations of initial value problems for the PDE (1.2). These are designed to test the map of the Riemann solver, and to demonstrate wave interactions predicted by the hyperbolic theory. However, as indicated earlier, surface tension can be expected to set a length scale for the interaction of waves that can be a factor in the selection of long time wave-like structure. Specifically, when there are two asymptotic structures for the same upstream and downstream heights, the selection by the PDE can depend on surface tension, resulting in disagreement with the prediction of the hyperbolic theory. The numerical results of Subsection 4.2 demonstrate that this effect is eliminated as the surface tension parameter γ approaches zero, so that the hyperbolic prediction is born out for small enough γ.

4.1 Numerical Solutions of the ODE

In Section 3, we established that the solution space for system (3.12) has six invariant manifolds, namely the stable manifold W^S and the unstable manifold W^U for each of the three equilibria, B, M and T. The manifolds have a complex structure in phase space (h, h', h''), so it is simpler to consider the intersections of these manifolds with Poincaré sections, i.e., plots of (h', h'') for a fixed value of h. For convenience, we label these intersections with the same labels W^S, W^U, even though the dimension drops by one. To compute intersections of the manifolds with the chosen Poincaré section, we employ LSODE[6] to integrate the ODE system along numerous trajectories, chosen by varying the initial data carefully. Computational issues pertaining to these calculations are discussed in [11].

[6]The Livermore Stiff ODE Solver, with an implicit Adams method and an adaptive time step.

To generate the kinetic relation and nucleation condition described in Section 3, we distinguish between two cases, which we refer to as the *jump-down* and *jump-up* cases. In the jump-down case, we consider trajectories from M or T to B, whereas in the jump-up case, the trajectories join B or M to T. Note that trajectories from M to T or B correspond to classical waves; trajectories from T to B are undercompressive waves, and trajectories from B to T are reverse undercompressive waves [18].

For the **jump down** case, we consider $0 < h_b < 1/3$, and plot intersections with the Poincaré section of the two dimensional unstable manifold $W^U(M)$ of M, the two dimensional stable manifold $W^S(B)$ of B, and the one dimensional unstable manifold $W^U(T)$ of T. Since we are focused on trajectories connecting to B, we choose a Poincaré section between B and M; after some experimenting, it is found to be convenient to take the section at $h = (2h_m + h_b)/3$, a weighted average based on the fact that h_b may be small, and therefore close to the singular point $h = 0$. Moreover, since we are considering jump-down trajectories, we restrict attention to intersections of the three manifolds at values of (h, h', h'') for which $h' < 0$. The structure of the manifolds (shown in Fig. 4.5) is that the curve representing $W^S(B)$ is nearly straight in the domain of interest, while $W^U(M)$ has a spiral terminating in the point representing one connected component of $W^U(T)$ (The other component has h increasing.) The spiral $W^U(M)$ can intersect the curve $W^S(B)$ in any number of points, each point representing a trajectory from M to B. When $W^U(T)$ lies on $W^S(B)$, there is a trajectory from T to B. Computations are performed by fixing h_b (as in Theorem 3.1), and varying h_m. The third equilibrium is calculated from $h_t = 1 - h_m - h_b$.

The *Kinetic Relation* $h = h^K(h_b)$ is the value of h_t for which $W^U(T)$ lies in $W^S(B)$ (see Fig. 4.5(b)), so that there is a trajectory from T to B (indicating an undercompressive traveling wave solution of the PDE). In the results of Figure 4.5, the value of h_m is tuned until we have $h = h^K(h_b)$ to two decimal places.

The *Nucleation Condition* $h = h^N(h_b)$ is the value of h_m for which $W^U(M)$ and $W^S(B)$, are tangent, and in the Poincaré section intersect only at one point (see Fig. 4.5(b)).[7] As for the kinetic relation, in Figure 4.5, the value of h_m is tuned until we have $h = h^N(h_b)$ to two decimal places. For larger values of h_m, the two manifolds are separated, so that there are no traveling waves from h_m or from h_t to this value of h_b. In this sense, the (double) orbit from M to B represented by the tangential intersection is the final orbit from M to B, as indicated in Table 4.1.

For the **jump-up** case, data for the kinetic relation and nucleation condition are gathered in an analogous manner, but in a different part of phase space. Specifically, the Poincaré section is chosen between M and T, at $h = (h_m + h_t)/2$, and we record intersections with $h' > 0$ (see Fig. 4.6). For these solutions, we are concerned with the spiral at the other end of $W^U(M)$, which has $W^U(B)$ at its center. The jump-up case is different from the jump-down case in that h_b is now the upstream height, and for the Riemann solver we want data for the kinetic relation and nucleation condition as functions of the downstream height. We again fix a value of h_b (as in Theorem 3.1) in the interval $0 < h_b < 1/3$, and vary h_m. As a result, we obtain *kinetic relation* data in the form $h = (h^K)^{-1}(h_b)$, the value of h_t for which $W^U(B)$ lies in $W^S(T)$, so that there is a trajectory from B to T (indicating a reverse undercompressive traveling wave solution of the PDE). Similarly, the *nucleation condition* corresponds to a function $h = \tilde{h}_m(h_b)$, the value of h_m for which $W^U(M)$ and $W^S(T)$ are tangent,

[7] Note that these manifolds have points of tangency for other values of h_m; the additional property of having a unique intersection defines the value of h_m uniquely, an assertion that has not been proved analytically, only observed numerically.

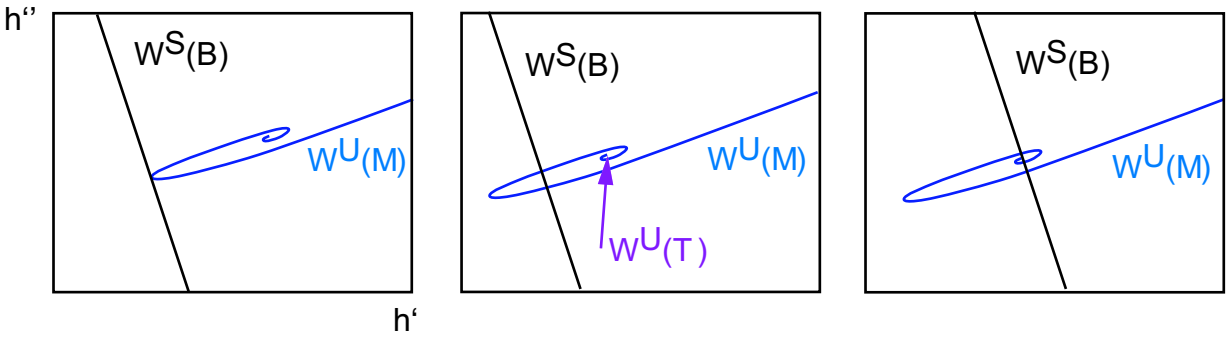

(a) Nucleation Condition (b) Two orbits from M to B (c) Kinetic Relation.

Figure 4.5: Poincaré Sections: Jump-down case.

	Kinetic Relation	Nucleation Condition
Jump-down	$T \to B$ (undercompressive)	final $M \to B$ orbit
Jump-up	$B \to T$ (reverse undercompressive)	final $M \to T$ orbit

Table 4.1: Relationship between jump-up/down cases, orbits, and types of wave.

and in the Poincaré section intersect only at one point. Figure 4.7 is a map of the Riemann solver

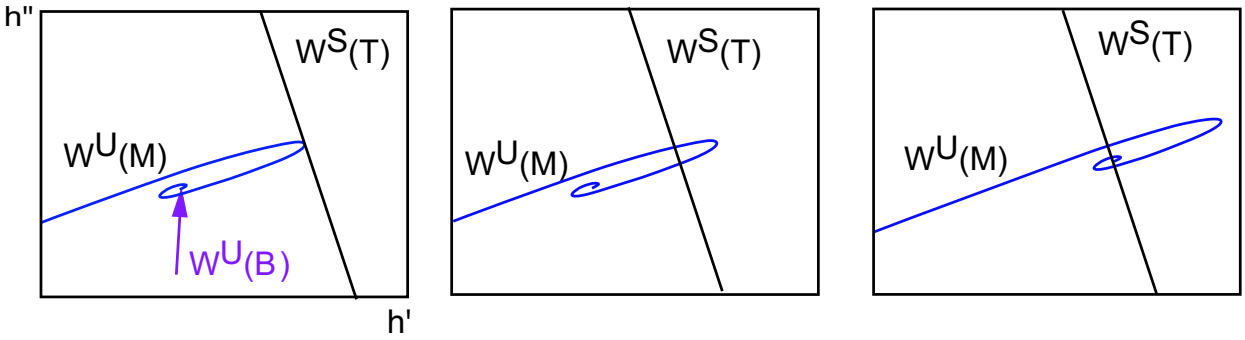

(a) Nucleation Condition (b) Two orbits from M to T (c) Kinetic Relation.

Figure 4.6: Poincaré Sections: Jump-up case.

that includes the computed kinetic relation and nucleation condition. To generate the curves as shown in the figure, the data for the jump-up case has to be processed, since h_b is on the left of jump-up waves, and the curves are graphs of functions of h_R. For the kinetic relation, this simply involves inverting the data, but for the nucleation condition, we plot the pairs of points $(h_R, \tilde{h}_m(h_b))$, where $h_R = 1 - h_b - \tilde{h}_m(h_b)$. That is, the nucleation curve $h = h^N(h_R), 1/3 < h_R < 1$ is plotted parametrically in Fig. 4.7. Somewhat surprisingly, the data from the jump-up and jump-down cases combine into smooth curves across the inflection point. As predicted by the theory of Section 3, the curves in the jump-up case approach the corner $(0, 1)$ of the domain, whereas the jump-down curves (with $h_R < 1/3$) seem not to approach a corner of the domain.

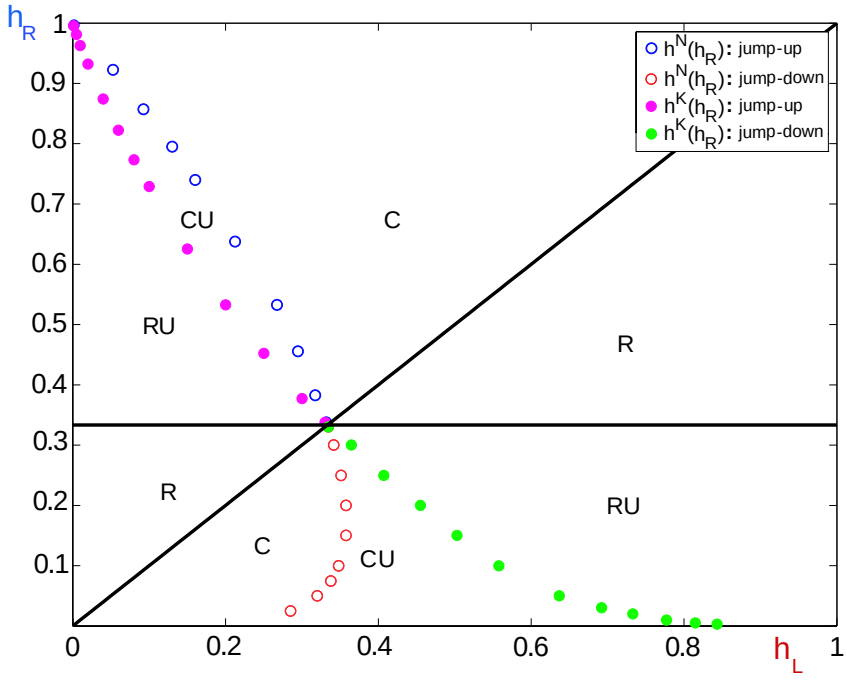

Figure 4.7: Numerical Map of the Riemann Solver. C: classical shock, U: undercompressive shock; R: rarefaction wave.

4.2 PDE Numerical Solutions

To solve the one-dimensional parabolic partial differential equation, $h_t + f(h)_x = -\gamma(h^3 h_{xxx})_x$ we employ a Crank-Nicolson finite difference scheme with an adaptive timestep. Simulations are performed on domains of varying lengths, with a mesh width $\Delta x = 0.002$. Boundary conditions were chosen as $h = h_L, h = h_R$ at the left and right edges of the domain, respectively, together with $h_x = 0$ at each end. Smooth initial data were chosen to approximate piecewise constant functions, using hyperbolic tangents with width δ chosen to be five times the mesh width, so that each discontinuity is smoothed over approximately five grid points.

We ran numerical simulations of the PDE (1.2) to test the Riemann solver, the nucleation condition, and to check that the evolution of waves for the equation with small surface tension mimics the prediction of the hyperbolic theory. Finally, we investigated the extent to which larger surface tension affects the evolution in a way not predicted by the hyperbolic theory.

In Figure 4.8 we show results from taking monotonic initial data that is a smoothed jump between values of h_L, h_R chosen from each of the eight regions in the Riemann solver map. The resulting solutions clearly show the structure indicated on the map. (In the Figure, we took two values of $h_R : h_R = 0.1, 0.6$, and chose four values of $h_L : h_L = 0.05, , 0.2, 0.4, 0.75$ so that the eight values of (h_L, h_R) lie in the eight different regions of Fig. 4.7.) Note that in the figure, the vertical scales are different in different plots to aid visualization of the solutions. The initial jump is positioned in the center of the domain when $h_L > 2/3$. In those cases, the characteristic speed at h_L is negative, and the resulting rarefaction wave propagates backwards as well as forwards. In all other cases, the initial jump is near the left end of the domain and the waves propagate to the right (i.e., with

positive speed).

For monotonic initial data, we tested the nucleation condition for the jump-down case by fixing $h_R = 0.1$ and varying h_L near the nucleation value $h_L = h^N(0.1) = 0.348$. For $h_L = 0.346$ (just below nucleation), the result was a compressive (classical) wave similar to that in Fig. 4.8 with $h_L = 0.2$ (well below nucleation). For $h_L = 0.350$ (slightly above nucleation), the initial data nucleated into classical and undercompressive waves that separated, as in Fig. 4.8 in which $h_L = 0.4$ (i.e., well above nucleation). However, the double wave structure took much longer to appear when $h_L = 0.350$ than for $h_L = 0.4$, the latter value being further from the nucleation threshold $h_L = 0.348$.

Next, we took non-monotonic initial data shown schematically in Figure 4.9 . The positioning of the various heights is arranged so that the solution of the Riemann problem with data h_L, h_R is a single wave, whereas the prediction of the hyperbolic theory is a two-wave structure (see Fig. 4.11).

For non-monotonic jump-down initial data with the ridge at h_0 well above the nucleation value, we explored what width of initial ridge was necessary to nucleate an undercompressive wave for $\gamma = 1$. In Fig. 4.10(a), we show the short-time behavior of a solution converging to a compressive wave. Clearly, the two initial discontinuities interact almost immediately; the width of the ridge is too narrow to allow the undercompressive wave to nucleate. The final (right-most) profile in the figure is included to show the shape of the compressive traveling wave clearly.

In Fig. 4.10(b), we take the same steps in the initial data, but space them further apart. In this case, the jump-down discontinuity has time to resolve into two waves before the single wave approaching from the left can interfere. The solutions of the two Riemann problems are clearly seen, together with the interaction of the classical waves, leading finally to the two-wave structure predicted by the hyperbolic theory. In the figure, an intermediate profile is emphasized, to show the three waves, in addition to the solution at the final time, showing the two-wave structure. The entire evolution is consistent with the hyperbolic theory, as can be seen by tracking the sequence of Riemann problem solutions. A schematic of the constant states and the chords joining them in the graph of f is shown in Fig. 4.11 to represent the wave interactions. Note that the two waves constituting the final state, a compressive wave from h_L to $h^K(h_R)$ and an undercompressive wave from $h^K(h_R)$ to h_R, have almost the same speed, so that the final ridge broadens quite slowly. The other two chords shown in the graph represent the two compressive waves, from h_L to h_0, and from h_0 to $h^K(h_R)$. These waves have quite different speeds, so that they meet rather quickly.

Let us argue that the wider ridge corresponds to a smaller value of the surface tension parameter γ. For any $\gamma > 0$, the variables in equation (1.2) can be scaled so that γ is eliminated, so that effectively, $\gamma = 1$. Consider piecewise constant initial data $h_w(x)$ with a single ridge of width w extending from $x = 0$ to $x = w > 0$. Note that $h_w(ax) = h_{w/a}(x)$ for any $a > 0$. For $\epsilon > 0$, let $h^\epsilon_w(x,t)$ denote the solution of (1.2) with $\gamma = \epsilon^3$ and $h^\epsilon_w(x,0) = h_w(x)$. It is easy to check that

$$h^\epsilon_w(x,t) = h^1_{w/\epsilon}(x/\epsilon, t/\epsilon),$$

where $h^1_{w/\epsilon}(x,t)$ solves equation (1.2) with $\gamma = 1$, and with initial data

$$h^1_{w/\epsilon}(x,0) = h_{w/\epsilon}(x).$$

The interpretation we need is that for $0 < \epsilon < 1$, if we solve equation (1.2) with $\gamma = 1$ and initial data of width $w/\epsilon > w$, then the result has the same shape (and is the same after scaling x, t) as

the result of solving the PDE with $\gamma = \epsilon^3 < 1$, and initial data of width w. This scaling provides a check of the numerical algorithm, as narrower initial widths require a finer mesh to capture all the structure of the solution.

The trend of more separated initial jumps corresponding to smaller γ makes sense when considering the limit $\gamma = 0$, where the equation is hyperbolic. Then the width is only relevant to the extent that it affects the time between wave interactions. In terms of short-time behavior, the width is effectively infinite since adjacent jumps do not influence each other until the first time of interaction. For general initial data (not just nearly piecewise-constant data), we might see different long-time behavior depending on γ, as well as the specific choice of data. However, for fixed initial data close to piecewise-constant, the above argument suggests that there is a value $\gamma_0 > 0$ with the property that solutions will be unchanged in long-time structure for all $\gamma < \gamma_0$.

In Figure 4.12 we show further transients in the evolution from non-monotonic initial data. We take $h_L = 0.265, h_0 = 0.29$ and $h_R = 0.025$. This time, the middle value h_0 is only slightly above nucleation ($h^N(0.025) = 0.285$). Consequently, although the front discontinuity (between h_0 and h_R) would generate a two wave structure if the other discontinuity were not in the initial data, the development of this structure would take a long time. In the simulation it is clear that, even though the width of the initial ridge is moderately large, the trailing rarefaction wave catches up to the leading structure before the two-wave profile has had time to emerge. Notice that the maximum height is still increasing when the trailing wave catches up; the subsequent interaction causes the maximum to fall eventually, and the PDE seeks out the traveling wave between h_L and h_R, whose maximum is above the nucleation threshold, but far from the left state ($h^K(0.025) = 0.715$) of the undercompressive wave (seen in Fig. 4.10(b)) predicted from the hyperbolic theory.

5 Conclusions

In this paper, we have made the connection between a new theory of scalar conservation laws, and the fourth order PDE representing thin film flow driven by competing forces. The connection involves extracting information about traveling wave solutions of the fourth order PDE in order to formulate a suitable kinetic relation and nucleation condition. These conditions are incorporated into the Riemann solver, which selects a unique weak solution of the Riemann problem, the building block of solutions of initial value problems for hyperbolic conservation laws. Numerical simulations then explore the extent to which the hyperbolic theory, augmented with this small amount of information from the fourth order PDE, actually predicts the behavior of solutions of the fourth order equation.

The critical test is that in the hyperbolic theory, the selection of long-time behavior depends in a subtle way on the choice of initial condition. While this is faithfully reproduced by the fourth order PDE when jumps in the initial data are well separated, when they are not, the surface tension can give short-time wave interactions not predicted by the hyperbolic theory, leading to long-time behavior at variance with the hyperbolic theory. Equivalently, the hyperbolic theory reproduces the long-time behavior accurately, provided the surface tension is sufficiently small.

6 Acknowledgements

The research of this paper was supported by the National Science Foundation grant DMS-0244491, and by the Isaac Newton Institute, Cambridge University. We are grateful to Ryan Haskett for helpful discussions, and assistance with the PDE simulations.

References

[1] R. Abeyaratne and J.K. Knowles, Kinetic relations and the propagation of phase boundaries in solids. Arch. Rational Mech. Anal. **114** (1991), 119–154.

[2] A. L. Bertozzi, A. Münch, and M. Shearer, Undercompressive Shocks in Thin Film Flows. Physica D, **134** (1999), 431-464.

[3] A. L. Bertozzi and M. Shearer, Existence of undercompressive traveling waves in thin film equations, SIAM J. Math. Anal., **32** (2000), 194-213.

[4] R. Buckingham, M. Shearer, and A. L. Bertozzi, Thin film traveling waves and the Navier slip condition, SIAM J. Appl. Math. **63** (2003), 722-744.

[5] E. A. Cox and A. Kluwick, Waves and nonclassical shocks in a scalar conservation law with nonconvex flux, Z. angew. Math. Phys. **52** (2001) 924949.

[6] D. Jacobs, W. McKinney, and M. Shearer, Traveling wave solutions of the modified Korteweg-De-Vries Burgers equation, J. Differential Equations **116** (1995), 448–467.

[7] S. Kruzkov, First order quasilinear equations with several space variables, Math. USSR Sb. **10** (1970), 217–243.

[8] P.D. Lax, Hyperbolic Systems of Conservation Laws II, Comm. Pure Appl. Math. **10** (1957), 537-566.

[9] P.G. LeFloch and M. Shearer, Nonclassical Riemann solvers with nucleation. Isaac Newton Institute for Math. Sciences preprint. Submitted to Proc. A Roy. Soc. Edinburgh.

[10] P.G. LeFloch, **Hyperbolic systems of conservation laws: The theory of classical and nonclassical shock waves,** Lectures in Mathematics, ETH Zürich, Birkhäuser, 2002.

[11] R. Levy and M. Shearer, Comparison of Two Dynamic Contact Line Models for Driven Thin Liquid Films. Euro. J. Appl. Math., submitted.

[12] O. Oleinik, Discontinuous solutions of nonlinear differential equations, Amer Math Soc. Transl. Ser. 26 (1963), 95–172.

[13] K. Radhakrishnan and A. Hindmarsh. Description and use of LSODE. NASA ref. pub. 1327. LLNL Report UCRL-1D-113855. March 1994. www.llnl.gov/CASC/nsde/pubs/u113855.pdf

[14] M.R. Schulze and M. Shearer, Undercompressive shocks for a system of hyperbolic conservation laws with cubic nonlinearity. J. Math. Anal. Appl. **229** (1999), 344–362.

[15] T.M. Segin, B.S. Tilley and L. Kondic, On undercompressive shocks in constrained two-layer flows, Physica D, submitted.

[16] M. Slemrod, Admissibility criteria for propagating phase boundaries in a van der Waals fluid. Arch. Rational Mech. Anal. **81** (1983), 301–315.

[17] M. Shearer, The Riemann problem for a class of conservation laws of mixed type. J. Differential Equations **46** (1982), 426–443.

[18] J. Sur, A. L. Bertozzi, R. P. Behringer, Reverse undercompressive shock structures in driven thin film flow, Phys. Rev. Lett. **90** (2003), 126105.

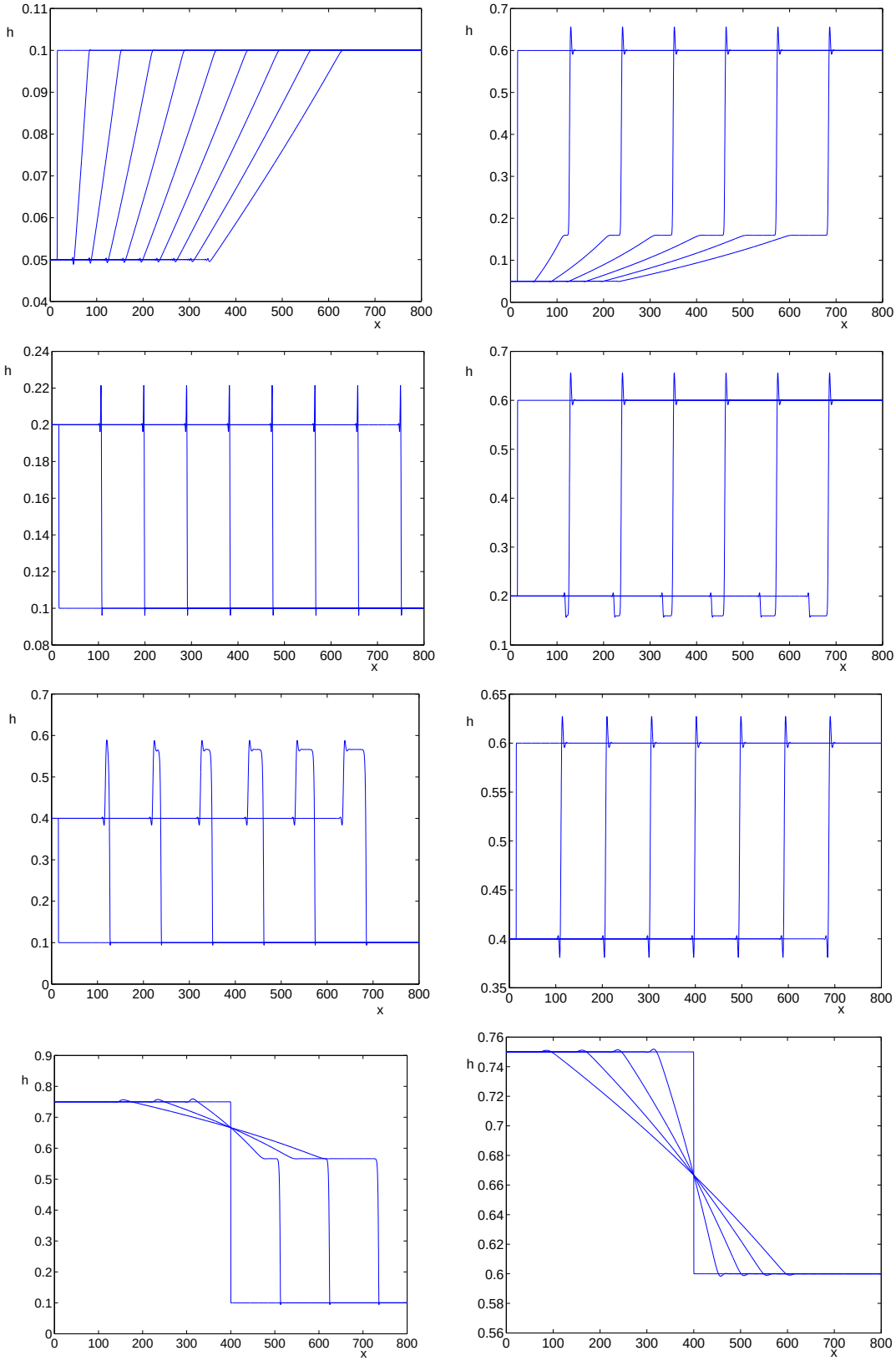

$h_R = 0.1$ $h_R = 0.6$

Figure 4.8: Riemann Problem Solutions; $h_L = 0.05, 0.2, 0.4, 0.75$.

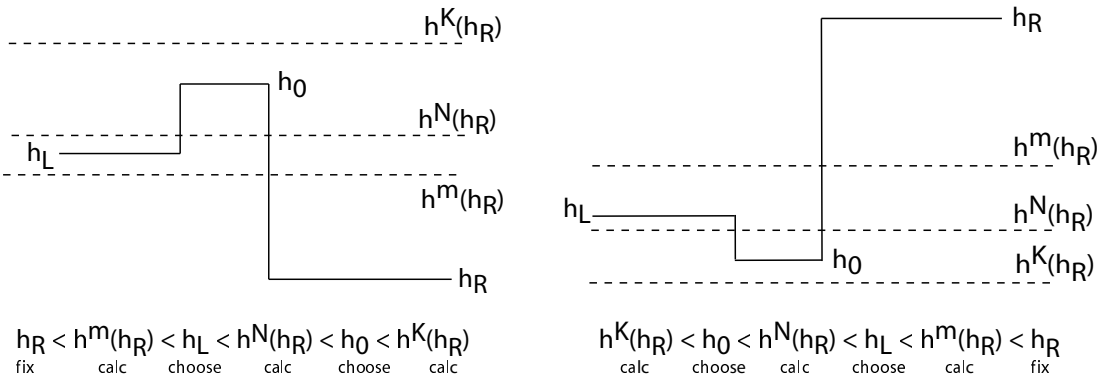

(a) Jump-down case (b) Jump-up case.

Figure 4.9: Non-monotonic initial data.

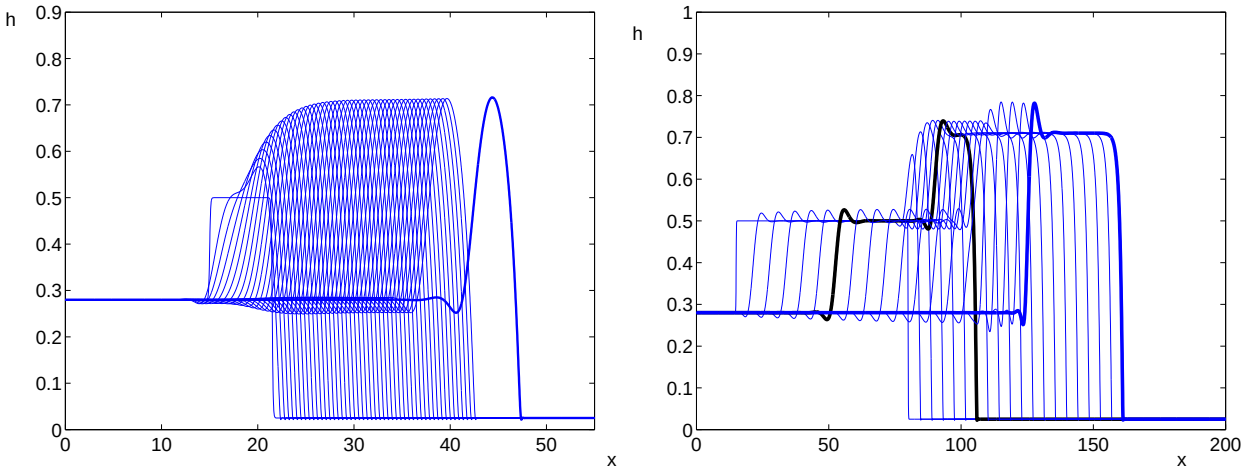

(a) Narrow ridge (b) Wide ridge.

Figure 4.10: Non-monotonic initial data. $h_L = 0.28 < h^N(h_R) = 0.285; h_R = 0.025$.

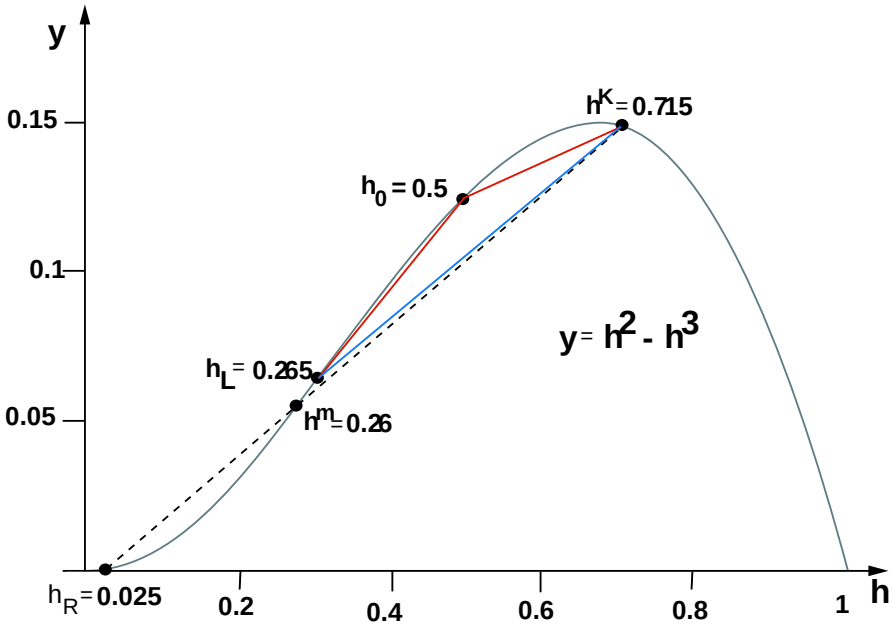

Figure 4.11: Tracking waves in the flux function.

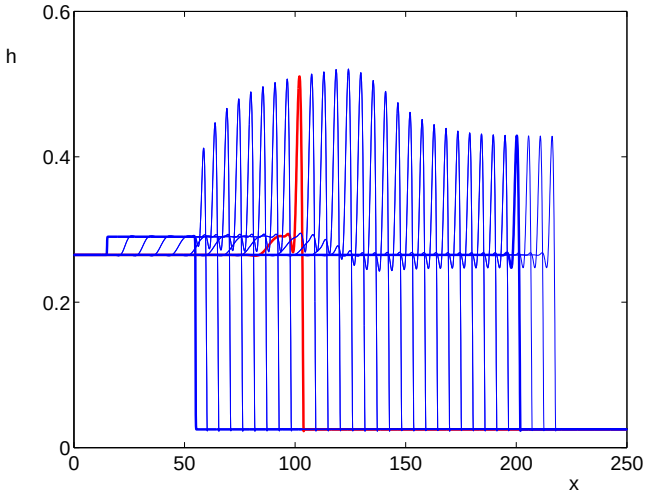

Figure 4.12: Transients and wave interactions preventing nucleation.
$h_L = 0.265, h_0 = 0.29 > h^N(h_R) = 0.285, h_R = 0.025$.